

1 The imbricated foreshock and aftershock activities of
2 the Balsorano (Italy) M_w 4.4 normal fault earthquake
3 and implications for earthquake initiation

4 H. S. Sánchez-Reyes¹, D. Essing¹, E. Beaucé², P. Poli¹¹

5 ¹*Institute of Earth Sciences, University Grenoble Alpes, Grenoble 38100, France*

6 ²*Department of Earth, Atmospheric, and Planetary Sciences, Massachusetts Institute of*
7 *Technology, Cambridge, MA, United States*

8 ^{*}*Corresponding author: hugo.sanchez-reyes@univ-grenoble-alpes.fr*

⁹ **Key words:**

¹⁰ • earthquake initiation process

¹¹ • earthquake sequence

¹² • spatio-temporal evolution

¹³ **Key points:**

¹⁴ • The analysis of the 2019 Balsorano earthquake sequence reveals that imbricated com-
¹⁵ plex processes occur before and after the main earthquake

¹⁶ • Clear differences between foreshocks and aftershocks are highlighted by the distinct
¹⁷ spatio-temporal patterns unraveled by our analysis

¹⁸ • These results demonstrate that simple earthquake preparation models are not suitable
¹⁹ enough to correctly mimic the observed complex reality

Abstract

Foreshocks in the form of microseismicity are among the most powerful tools to study the physical processes that occur before main earthquakes. However, their detection and precise characterization is still sparse, especially for relatively small earthquakes ($M_w < 5$). We present here a detailed foreshock analysis for the November 7, 2019, Balsorano (Italy) normal fault earthquake (M_w 4.4). To improve the detection of the microseismicity before and after the mainshock, we use six three-component broadband receivers at distances of less than 75 km from the targeted seismicity, through template matching. To improve the understanding of the physical mechanism(s) behind the earthquake initiation process, as well as other accompanying phenomena, we also detail the spatio-temporal evolution of the sequence associated to this medium-sized earthquake, using waveform clustering and hypocenter relocation. Clear differences between foreshocks and aftershocks are revealed by this analysis. Moreover, five distinct spatio-temporal patterns associated to the different seismic activities are revealed. The observed spatio-temporal behavior shown by the foreshocks highlights a complex initiation process, which apparently starts on an adjacent unmapped antithetic fault. Finally, the aftershock activity comprises four different clusters with distinct spatio-temporal patterns, which suggests that each cluster in this sequence has a distinct triggering mechanism.

Introduction

The detection of signals that can inform us about an incoming earthquake is fundamental to build physical models that mimic the processes behind the triggering of earthquakes. Over the last 25 years, numerous studies have reported a wide range of observations that appear to be connected with the physics that precedes large seismic events (*e.g.* [Rikitake, 1975](#); [Jones and Molnar, 1979](#); [Molchanov et al., 1998](#); [Eftaxias et al., 2000](#); [Virk and Walia, 2001](#); [Singh et al., 2010](#); [De Santis et al., 2019](#); [Jones, 1985](#); [Abercrombie and Mori,](#)

1996; Felzer et al., 2004; Dodge et al., 1996; Ellsworth and Bulut, 2018; Yoon et al., 2019; Reasenberg, 1999; Ruiz et al., 2017, 2014a). Among these, the more significant ones have been based on seismological characterization of foreshock sequences and their relationships with mainshocks (*e.g.* Jones, 1985; Abercrombie and Mori, 1996; Reasenberg, 1999; Felzer et al., 2004; Dodge et al., 1996; Ellsworth and Bulut, 2018; Yoon et al., 2019; Ruiz et al., 2017). Foreshocks are thus one of the most useful tools to understand the physics of earthquake initiation in real faults (Brune, 1979; Abercrombie and Mori, 1996; Malin et al., 2018). Therefore, it is important to improve foreshock observations and characterization, even for frequent medium-sized events (*i.e.* $M_w < 6$), as these might share similar physical processes with larger events. These improved observations shed new light on the physical processes that occur during the triggering of earthquakes and will drive future research that focuses on theoretical and numerical models to better characterize earthquake occurrence in real and complex faults.

Earthquake initiation (*e.g.* Kato et al., 2012; Schurr et al., 2014; Tramutoli et al., 2015) and earthquake nucleation/triggering (*e.g.* Dieterich, 1992; Ellsworth and Beroza, 1995; Rubin and Ampuero, 2005) are two different, and perhaps overlapping, phases of the seismic cycle. While the first is understood to occur over the longer term preceding a large event (*i.e.*, days or months, to years), the second occurs some minutes to seconds before the main event. Both phases, however, can be explained under the Dieterich model (1994), which relates the seismicity rate to the stressing history through a rate-and-state constitutive law. For earthquake initiation in particular for real faults, two main hypotheses are currently used to explain this process. Some authors argue that a mainshock is a consequence of a cascade process, with stress transfer in-between events, which eventually trigger the large event (*e.g.*, Dodge et al., 1996; Ellsworth and Bulut, 2018; Yoon et al., 2019). Alternatively, the initiation of an earthquake can be understood as an aseismic process that weakens the pre-existing asperities, until a larger rupture is promoted (Dodge et al., 1996; Bouchon et al., 2011; Tape et al., 2018). In the latter case, foreshocks result from the activation of brittle

asperities by the surrounding slip processes. However, intermediate models that involve both triggering and aseismic slip are likely for complex faults (*e.g.* [McLaskey, 2019](#)). This complexity might result from fault heterogeneity (*e.g.*, variable stress, frictional properties) and promote imbricated sequences of foreshocks and aseismic slip (*e.g.*, [Dublanchet, 2018](#)).

The monitoring of foreshocks is today routine in laboratory experiments ([Zang et al., 1998](#); [Goebel et al., 2012](#); [Renard et al., 2019](#), and references therein), while studies that focus on large earthquakes remain relatively sparse (*i.e.*, $M_w > 6$) (*e.g.*, [Mogi, 1963](#); [Abercrombie and Mori, 1996](#); [Kato et al., 2012](#); [Chen and Shearer, 2013](#); [Bouchon et al., 2013](#); [Ruiz et al., 2014b,a](#)). However, the recent improvements to seismological monitoring systems around active faults have now provided detailed analysis of foreshocks that precede the more frequent small-magnitude earthquakes ($M_w < 6$) (*e.g.*, [Savage et al., 2017](#); [McMahon et al., 2017](#); [Malin et al., 2018](#)). One intriguing feature that has emerged from these last more recent studies is the increased complexity (*i.e.*, fault interactions, volumetric processes) that have been revealed through the availability of better data (*e.g.*, near-fault receivers) and more advanced detection methods (*e.g.*, template matching) to study foreshocks. This complexity might challenge the actual laboratory scale and theoretical models, which treat earthquake initiation as simple physical processes that occur in smooth fault planes ([Dieterich, 1992](#); [Marone, 1998](#); [Rubin and Ampuero, 2005](#); [Liu and Rice, 2005](#)). The necessity for high-resolution characterization of foreshocks based on good data and advanced data processing techniques was also suggested by a meta-analysis carried out by [Mignan \(2014\)](#), which indicated resolution-dependent bias for earthquake initiation models that were resolved using seismological data.

To shed new light on the physical processes that occur before relatively small earthquakes, we study here the medium-sized (M_w 4.4) Balsorano normal fault earthquake and its foreshock-aftershock sequence (Fig. 1). The Italian National Institute of Geophysics and Volcanology (*Istituto Nazionale di Geofisica e Vulcanologia*; INGV; [online catalog](#)) reported that the main event of this sequence occurred on November 7, 2019 (17:35:21.18 UTC), ap-

proximately 4 km southeast of Balsorano city in central Italy (Fig. 1). The hypocenter of this main event was located relatively deep in the crust (~ 15 km), close to the transition zone between the upper and lower crust (10-20 km in depth), where the brittle locked fault transitions into the ductile regime zone (Doglioni et al., 2011). Below this depth, the lower crust is relatively seismically silent (Doglioni et al., 2011). According to a geological study of the location of the main event and its focal mechanism (Supplementary Material Table S1), this event ruptured the Liri fault (Roberts and Michetti, 2004), which is one of the major active normal faults mapped in this region. This structure accommodates the low extension rate observed in this region (*i.e.*, a few millimeters per year) (Hunstad and England, 1999; Westaway, 1992; D’agostino et al., 2001; Roberts and Michetti, 2004).

[Figure 1]

In addition to the mainshock of November 7, 2019, 135 events occurred close to the epicenter of the main event from October 22 to November 15, 2019 (which included 25 foreshocks). Starting from these cataloged events, we study here the ‘anatomy’ of the foreshocks and aftershocks, and their relationships with the main event. With this aim, continuous data from six three-component stations at less than 75 km from the mainshock epicenter are used (Fig. 1; Supplementary Materials Table S2). The continuous waveforms recorded are analyzed using template matching techniques (Gibbons and Ringdal, 2006; Shelly et al., 2007) to detect smaller events and thus to expand upon the available seismic catalog. The detected events are then relocated using the double-difference method (Waldhauser, 2001), to reveal the geometry of the main fault and to obtain new insights into the fault-slip behavior(s) before and after the main seismic event. Furthermore, through waveform clustering, we isolate families of earthquakes that are representative of different physical processes that occur in the pre- and post-mainshock period. This combination of detection, relocation, and waveform clustering reveals an imbricated seismic sequence where several faults were activated, and with clear differences in the spatio-temporal properties

126 of the foreshocks and aftershocks.

127 Methods

128 **Template matching:** The analysis starts by extending the INGV seismic catalog using the
129 template matching approach ([Gibbons and Ringdal, 2006](#)). From the 135 events reported
130 by the INGV online catalog , where 25 events are identified as foreshocks, we retain only
131 the events with available P-wave and S-wave picks for all of the six stations used. We then
132 extract 4 s of signal, starting 1 s before the phase arrival time from the band-pass filtered
133 data (5-20 Hz). Using the pre-picked signals, we estimate the signal-to-noise ratio and
134 retain as templates only those events with a signal-to-noise ratio >3 at all of the stations.
135 With this data selection, 23 events are obtained (including three foreshocks) that are the
136 templates used for scanning the continuous data (Supplementary Materials Table S4). We
137 use three-component data with P waves extracted from the vertical component, and S waves
138 extracted from the East and North components.

139 In all, 28 days of continuous data are processed, from October 22 (*i.e.*, 16 days before
140 the mainshock) to November 15, 2019, using the fast matched filter algorithm from [Beaucé](#)
141 [et al. \(2017\)](#). The detection thresholds are set to 12 times the daily median absolute devi-
142 ation of the summed correlation coefficients over the array of stations. Finally, consecutive
143 detections with differential times of <3 s are removed (*i.e.*, the time difference between two
144 estimated origin times).

145 The final catalog contains 714 events (166 foreshocks, 547 aftershocks), which represents
146 ~ 6 -fold the number of events in the initial catalog. To estimate the magnitudes of the
147 newly detected events, we use the average root mean square in the time window containing
148 the S waves over all of the stations and components. Least-square fitting is then used
149 to obtain a linear model that relates the logarithmic of the root mean square of the 23
150 templates and their local magnitudes from the INGV catalog. This model is then used to

estimate the magnitude of the newly detected events. A summary of the event occurrences in time together with their magnitudes is shown in Figure 2.

[Figure 2]

Waveform-based clustering: Clustering is widely used in seismology to recognize patterns in spatio-temporal events, which include the identification of foreshock-aftershock sequences and stress evolution in time (*e.g.*, Kagan and Jackson, 1991; Wehling-Benatelli et al., 2013; Cesca et al., 2014; Ellsworth and Bulut, 2018). Here, we apply waveform similarity analysis (Cattaneo et al., 1999) to define groups of events that share similar locations and/or a common rupture mechanism (Kagan and Jackson, 1991; Wehling-Benatelli et al., 2013; Cesca et al., 2014; Ellsworth and Bulut, 2018; Cattaneo et al., 1999). For this, the full normalized waveforms are used, with a 4.5-s time window (starting 0.5 s before the P-wave arrival) that contains both the P phase and the S phase.

The waveforms of the 714 detected events recorded at the closest station to the epicenter (Fig. 1, VVLD) are then correlated with each other. The correlation matrix obtained (Fig. 3a) is used to estimate the distance (dissimilarity) metric to perform hierarchical clustering. The Ward minimum variance method is used (Ward Jr, 1963) with a distance threshold of 5.5 defined (Supplementary Materials Fig. S1: the largest separation observed from the dendrogram). This waveform similarity analysis highlights five different clusters, as shown in Figure 3b, c. As both the P waves and S waves are used for clustering, the resulting family members should share similarities in position and rupture mechanism (Kagan and Jackson, 1991; Wehling-Benatelli et al., 2013; Cesca et al., 2014; Ellsworth and Bulut, 2018; Cattaneo et al., 1999).

Relocation: We finally estimate the relative location between the detected events using the double-difference algorithm (HypoDD software; Waldhauser (2001)). The differential times of the P phases and S phases between events from the cross-correlation are estimated, with the retention of only the delays that are associated to correlation coefficients >0.6 .

We further limit the delays to 0.2 s. After discarding the event pairs that relate less than 3 P-wave and 3 S-wave highly correlated differential times (correlation coefficient, ≥ 0.6), the final number of 29859 pairs are kept and used in the relocation process.

For each newly detected event, we assume its initial location as the coordinates of the template that reports the highest correlation coefficient related to that event. In addition, we assume the estimated P-wave and S-wave picks obtained from our template matching analysis as the initial catalog information for the relocation. A velocity model for this region proposed by [Bagh et al. \(2007\)](#) is used in the relocation process (Supplementary Materials Table S3). Following previous studies ([Shelly and Hardebeck, 2019](#)), the inversion is performed with stronger weights to the initial information related to the P-wave and S-wave picks from the catalog (*i.e.*, from the template matching analysis), while the differential times from the waveform correlations control the final iterations. In the end, 689 of the 714 newly detected events are successfully relocated. The temporal and geometric patterns observed in this earthquake sequence are illustrated in Figures 4 and 5, and are further described in the following section.

[Figure 3]

Results and discussion

The time evolution of the detected events is shown in Figure 2. Of the 714 events, 166 are foreshocks (23%). Together with the temporal evolution, Figure 2a shows the spectrogram and the average spectral energy in a frequency band from 5 Hz to 20 Hz. The oscillation of this energy suggests variable noise levels in the study area, with lower noise during the night (Figure 2, shaded areas, for periods from 18:00 to 06:00). This noise variation is related to anthropogenic activity ([Poli et al., 020b](#)), and it is also observed for the other five receivers. This noise evolution will probably affect our detection performance. For

example, it is not clear if the reduced number of events observed prior to the mainshock is real or is a consequence of the higher noise level (Fig. 2b). We thus avoid discussing any issue related to pre-seismic quiescence here. However, with the geometric and clustering information derived above, we can still characterize some of the properties of the newly detected foreshocks and aftershocks, and gain insight into the physical processes that occur at the different stages of the sequence.

The results from the combination of waveform clustering and relocation strategies are summarized in Figures 4 and 5. For each cluster, the coefficient of variation (COV) is also estimated from the recurrence time of the events (Kagan and Jackson, 1991; Schoenball and Ellsworth, 2017). The COV indicates the level of the temporal clustering within each group (*i.e.*, how much the occurrence of future earthquakes depends on the occurrence of the past earthquakes): with $\text{COV}=1$ for random seismicity, and $\text{COV}>1$ for strong temporal clustering. The larger the COV, the more the earthquakes are interacting. Thus, it is important to note that events that happen together with a high COV mean that there is an intrinsically related interaction between them.

The temporal and spatial densities of the different clusters identified in this sequence are illustrated in Figure 4, where cluster 1 (green solid lines and dots) is mainly composed of foreshocks (161 of 209 events occurred before the mainshock). The events that form this family show the highest waveform similarity (Fig. 3a). In agreement with this waveform property, cluster 1 has high spatial density, with approximately 90% of its activity (193 of the 208 events) located within 0.5 km of the mainshock hypocenter (Figs. 4a and 5a). Cluster 1 also shows the highest temporal clustering ($\text{COV}=4.8$; Fig. 4a).

The next two families, as cluster 2 ($\text{COV}=3.0$; Figure 4b, blue solid lines and dots) and cluster 3 ($\text{COV}=2.9$; Figure 4c, magenta solid lines and dots), share similar temporal clustering values, but show differences with respect to their spatial densities. While approximately 90% of the events of cluster 2 are within 0.8 km of the hypocenter (136 of 151 events; Fig. 4b), cluster 3 has almost 90% of its activity (187 of 211 events) located over

228 a larger volume, as approximately 1.2 km from the mainshock location (Fig. 4c). Cluster
 229 4 (Figure 4d, brown solid lines and dots) is characterized by 90% of its activity within 0.6
 230 km of the mainshock hypocenter (53 of 59 shocks; Fig. 4d). The seismicity in this cluster
 231 is also characterized by high temporal clustering (COV=4.2). Cluster 5 (COV=2.2; Figure
 232 4e, red solid lines and dots) is the least temporally clustered, but with the second highest
 233 spatial density (after cluster 1), with 90% of its activity in a region 0.5 km from the main-
 234 shock hypocenter (66 of 73 events; Fig. 4e). A general spatial pattern of this sequence is
 235 the concentration of events close to the mainshock that occurred prior to it (110 foreshocks
 236 within 0.3 km) and the subsequent spread over a region >0.3 km during the aftershocks.

237 Figure 5 illustrates the geometric patterns related to each of the clusters, as defined
 238 by the relocation process. A remarkable pattern can be seen in Figure 5a: cluster 1 (*i.e.*,
 239 foreshocks) shows an antithetical orientation with respect to the assumed fault plane of
 240 the main event (Fig. 5a, map view and cross sections). In contrast, clusters 4 and 5 show
 241 nearly parallel orientations with respect to the assumed main fault plane (Fig. 5d, e, cross-
 242 sections, respectively). We also observe particular behavior for cluster 5, which is the only
 243 cluster where the activity is exclusively to the northeast of the mainshock hypocenter and
 244 on the footwall (Fig. 5e, map view and cross-sections). The events in cluster 5 follow an
 245 orientation that is parallel to the assumed main fault plane dipping angle (Fig. 5e, cross-
 246 section). In turn, cluster 3 has an activity that follows the orientation of the fault plane, but
 247 that spreads across the whole volume surrounding the fault plane (Fig. 5c, cross-sections).

248 [Figure 4]

249 [Figure 5]

250 The results of the spatio-temporal evolution for the identified clusters suggest complex
 251 evolution of the seismicity. Two fault planes are activated during the sequence, with fore-
 252 shocks primarily occurring on the antithetic fault plane (Fig. 5a, cross-section), similarly to

part of the foreshock activity that was observed for the L'Aquila normal fault earthquake (Chiaraluce et al., 2011). Relying only on our observations, it is hard to unravel which mechanism(s) might be responsible for the occurrence of the foreshocks, and thus the driving of the main event. For example, there are no exponential or power-law increments of events seen while approaching the main event (Papazachos, 1975; Kagan and Knopoff, 1978), which might suggest accelerating aseismic slip (Dodge et al., 1996; Bouchon et al., 2011; Tape et al., 2018). Neither are any spatial patterns seen (*e.g.*, migrations) that might suggest the same mechanism, or might alternatively indicate triggering by stress transfer (Dodge et al., 1996; Ellsworth and Bulut, 2018; Yoon et al., 2019). However, we clearly outline the differences between the foreshocks and aftershocks. In particular, the foreshocks occur in a more temporal clustered manner, and they are closer to the hypocenter of the main event (Fig. 4a). The compact and highly temporal clustered seismicity indicates strong event interactions, and favors stress transfer as the mechanism for foreshock occurrence (COV, Schoenball and Ellsworth, 2017).

Interestingly, the aftershock clusters also show different spatio-temporal behaviors between each other (Figs. 5b-e, 4b-e). The observed differences might be explained by different physical processes driving the aftershock occurrence. For example, the events in clusters 2 and 3 (Fig. 5b,c) spread in a volume around the fault. This spatial pattern is likely to result from stress redistribution, volumetric damage, and relaxation processes after the mainshock (Trugman et al., 2020). In contrast, clusters 4 and 5 follow the orientation of the main fault in a more compact volume around it (Fig. 5d,e), and their activity decays in a rapid manner (Fig. 4). This behavior might suggest that these latter clusters result from stress increments induced by the mainshock afterslip that occurs near the fault plane region in the few hours or days after the main event (Stein and Lisowski, 1983; Shen et al., 1994).

As in previous studies (McMahon et al., 2017; Savage et al., 2017; McMahon et al., 2019), we can see that this detailed analysis of seismic data reveals a complex and imbricated

earthquake sequence, for which the mainshock initiation is unlikely to result from only the evolution of physical properties (*e.g.*, stress, friction) on the main fault plane. Indeed the sequence begins through an interaction between the antithetic and main faults during the foreshock-mainshock sequences, similar to that observed for other events (Chiaraluce et al., 2011; McMahon et al., 2019). In normal faults, this behavior can be related to preseismic processes in the dilation wedge located in the hanging wall (Doglioni et al., 2011). The complexity of the sequence might also emerge from fluid involvement, which is known to have a significant role in the control of seismicity and its 'style' in the central Apennines (Antonoli et al., 2005; Poli et al., 2020a). The stress perturbations in the antithetic fault might have modified the local pore pressures, with fluid migration into the main fault, which would favor the occurrence of the main event (Doglioni et al., 2011).

Conclusion

By using a combination of high-resolution detection methods, precise relocation (*e.g.*, Gibbons and Ringdal, 2006; Waldhauser, 2001) and waveform clustering, we have unveiled the complexity of the sequences associated with the 2019 (M_w 4.4) Balsorano earthquake. We detect 714 events that comprise this sequence. These events are classified into five different seismic clusters. The differences between these clusters are highlighted by their distinct spatio-temporal properties that are unveiled by the waveform-based clustering analysis (Kagan and Jackson, 1991; Wehling-Benatelli et al., 2013; Cesca et al., 2014; Ellsworth and Bulut, 2018), and by their relative source locations (Waldhauser, 2001).

Our results highlight different behaviors between foreshocks and aftershocks. For example, foreshocks occur in a compact region near the mainshock hypocenter, and show high temporal clustering (Fig. 4a). The lack of repeating events (*i.e.*, highly correlated events with correlation coefficient >0.9), strong temporal clustering, and inter-event proximity might indicate that stress transfer triggering has the main role in driving the occurrence

of the foreshocks (Dodge et al., 1996). Nevertheless, there are no observations that can exclude aseismic slip. The foreshock activity mainly take place in an antithetic fault (Fig. 5a), which suggests that the initiation processes do not only occur on one fault plane, but involve larger volumes (Savage et al., 2017). This precursory antithetic activation has been observed in other normal fault events (Chiaraluce et al., 2011) and it can be expected in some gravity-driven normal fault models (Doglioni et al., 2011).

Furthermore, our analysis shows diversity for the aftershocks behavior. Indeed, four different clusters comprise the aftershock sequences. Two of these four are spread in a volume around the main fault (Fig. 5b,c), and might result from stress redistribution after the mainshock (*e.g.*, caused by volumetric damage and the relaxation processes; Trugman et al. (2020)). Given the rapid temporal decay of their activity and their compactness and spatial orientation, the remaining two clusters appear to be driven by rapid stress increments induced by the mainshock and afterslip that occur near the fault plane in the few days after the mainshock (Stein and Lisowski, 1983; Shen et al., 1994).

In summary, this study of foreshocks and aftershocks highlights that simple preparation models with evolution of stress and friction on a single fault plane are not suited to precisely explain the evolution of the seismicity we observe here for a real fault. A relatively large volume appears to be involved in the earthquake initiation, over a short time scale (~ 1 day). We further highlight how the full range of aftershocks is likely to be an ensemble average view of different processes, which will include afterslip, volumetric damage, and relaxation. Continuing to provide detailed information about foreshocks and their relationships to the mainshock and aftershocks also for relatively small events can help us to develop new and more realistic models that can provide better fitting of seismological observations and shed new light on the initiation of earthquakes in real faults.

Data and resources

The continuous seismic data used in this study are available at the Istituto Nazionale di Geofisica e Vulcanologia (INGV) seismological data center (http://cnt.rm.ingv.it/webservices_and_software/, last accessed, March 2020) and were downloaded using obspyDMT (<https://github.com/kasra-hosseini/obsipyDMT>, Hosseini and Sigloch (2017)). The fast matched filter (Beaucé et al., 2017) used in this study can be found at https://github.com/beridel/fast_matched_filter. Some plots were made using the Generic Mapping Tools version 4.5.14 (www.soest.hawaii.edu/gmt; Wessel and Smith (1998)). The event clustering was performed using Scikit-learn (<https://scikit-learn.org/stable/>; Pedregosa et al. (2011))

Acknowledgments

This research received funding from the European Research Council (ERC) under the European Union Horizon 2020 Research and Innovation Programme (grant agreement 802777-MONIFaults). Computations were performed using the University of Grenoble Alpes (UGA) High-Performance Computing infrastructures CIMENT (<https://ciment.univ-grenoble-alpes.fr>).

References

- Abercrombie, R. E. and Mori, J. (1996). Occurrence patterns of foreshocks to large earthquakes in the western united states. *Nature*, 381(6580):303–307.
- Antonioli, A., Piccinini, D., Chiaraluce, L., and Cocco, M. (2005). Fluid flow and seismicity pattern: Evidence from the 1997 umbria-marche (central italy) seismic sequence. *Geophysical Research Letters*, 32(10).
- Bagh, S., Chiaraluce, L., De Gori, P., Moretti, M., Govoni, A., Chiarabba, C., Di Bar-

tolomeo, P., and Romanelli, M. (2007). Background seismicity in the central apennines
of italy: The abruzzo region case study. *Tectonophysics*, 444(1-4):80–92.

Beaucé, E., Frank, W. B., and Romanenko, A. (2017). Fast matched filter (fmf): An
efficient seismic matched-filter search for both cpu and gpu architectures. *Seismological
Research Letters*, 89(1):165.

Bouchon, M., Durand, V., Marsan, D., Karabulut, H., and Schmittbuhl, J. (2013). The long
precursory phase of most large interplate earthquakes. *Nature geoscience*, 6(4):299–302.

Bouchon, M., Karabulut, H., Aktar, M., Özalaybey, S., Schmittbuhl, J., and Bouin, M.-P.
(2011). Extended nucleation of the 1999 mw 7.6 izmit earthquake. *science*, 331(6019):877–
880.

Brune, J. N. (1979). Implications of earthquake triggering and rupture propagation for
earthquake prediction based on premonitory phenomena. *Journal of Geophysical Re-
search: Solid Earth*, 84(B5):2195–2198.

Cattaneo, M., Augliera, P., Spallarossa, D., and Lanza, V. (1999). A waveform similarity
approach to investigate seismicity patterns. *Natural hazards*, 19(2-3):123–138.

Cesca, S., Şen, A. T., and Dahm, T. (2014). Seismicity monitoring by cluster analysis of
moment tensors. *Geophysical Journal International*, 196(3):1813–1826.

Chen, X. and Shearer, P. M. (2013). California foreshock sequences suggest aseismic trig-
gering process. *Geophysical Research Letters*, 40(11):2602–2607.

Chiaraluce, L., Valoroso, L., Piccinini, D., Di Stefano, R., and De Gori, P. (2011). The
anatomy of the 2009 l’aquila normal fault system (central italy) imaged by high resolu-
tion foreshock and aftershock locations. *Journal of Geophysical Research: Solid Earth*,
116(B12).

374 D’agostino, N., Giuliani, R., Mattone, M., and Bonci, L. (2001). Active crustal extension in
375 the central apennines (italy) inferred from gps measurements in the interval 1994–1999.
376 *Geophysical Research Letters*, 28(10):2121–2124.

377 De Santis, A., Marchetti, D., Pavón-Carrasco, F. J., Cianchini, G., Perrone, L., Abbattista,
378 C., Alfonsi, L., Amoruso, L., Campuzano, S. A., Carbone, M., et al. (2019). Precursory
379 worldwide signatures of earthquake occurrences on swarm satellite data. *Scientific reports*,
380 9(1):1–13.

381 Dieterich, J. (1994). A constitutive law for rate of earthquake production and its application
382 to earthquake clustering. *Journal of Geophysical Research: Solid Earth*, 99(B2):2601–
383 2618.

384 Dieterich, J. H. (1992). Earthquake nucleation on faults with rate-and state-dependent
385 strength. *Tectonophysics*, 211(1-4):115–134.

386 Dodge, D. A., Beroza, G. C., and Ellsworth, W. (1996). Detailed observations of califor-
387 nia foreshock sequences: Implications for the earthquake initiation process. *Journal of*
388 *Geophysical Research: Solid Earth*, 101(B10):22371–22392.

389 Doglioni, C., Barba, S., Carminati, E., and Riguzzi, F. (2011). Role of the brittle–ductile
390 transition on fault activation. *Physics of the Earth and Planetary Interiors*, 184(3-4):160–
391 171.

392 Dublanchet, P. (2018). The dynamics of earthquake precursors controlled by effective fric-
393 tion. *Geophysical Journal International*, 212(2):853–871.

394 Eftaxias, K., Kopanas, J., Bogris, N., KAPIRIS, P., ANTONOPOULOS, G., and VAROT-
395 SOS, P. (2000). Detection of electromagnetic earthquake precursory signals in greece.
396 *Proceedings of the Japan Academy, Series B*, 76(4):45–50.

397 Ellsworth, W. L. and Beroza, G. C. (1995). Seismic evidence for an earthquake nucleation
398 phase. *Science*, 268(5212):851–855.

399 Ellsworth, W. L. and Bulut, F. (2018). Nucleation of the 1999 izmit earthquake by a
400 triggered cascade of foreshocks. *Nature Geoscience*, 11(7):531–535.

401 Felzer, K. R., Abercrombie, R. E., and Ekstrom, G. (2004). A common origin for af-
402 tershocks, foreshocks, and multiplets. *Bulletin of the Seismological Society of America*,
403 94(1):88–98.

404 Gibbons, S. J. and Ringdal, F. (2006). The detection of low magnitude seismic events using
405 array-based waveform correlation. *Geophysical Journal International*, 165(1):149–166.

406 Goebel, T., Becker, T., Schorlemmer, D., Stanchits, S., Sammis, C., Rybacki, E., and
407 Dresen, G. (2012). Identifying fault heterogeneity through mapping spatial anomalies in
408 acoustic emission statistics. *Journal of Geophysical Research: Solid Earth*, 117(B3).

409 Hosseini, K. and Sigloch, K. (2017). Obspydmt: a python toolbox for retrieving and pro-
410 cessing large seismological data sets. *Solid Earth*, (5):1047–1070.

411 Hunstad, I. and England, P. (1999). An upper bound on the rate of strain in the central
412 apennines, italy, from triangulation measurements between 1869 and 1963. *Earth and*
413 *Planetary Science Letters*, 169(3-4):261–267.

414 Jones, L. M. and Molnar, P. (1979). Some characteristics of foreshocks and their pos-
415 sible relationship to earthquake prediction and premonitory slip on faults. *Journal of*
416 *Geophysical Research: Solid Earth*, 84(B7):3596–3608.

417 Jones, L. M. (1985). Foreshocks and time-dependent earthquake hazard assessment in
418 southern california. *Bulletin of the Seismological Society of America*, 75(6):1669–1679.

419 Kagan, Y. and Jackson, D. D. (1991). Long-term earthquake clustering. *Geophysical Journal*
420 *International*, 104(1):117–133.

421 Kagan, Y. and Knopoff, L. (1978). Statistical study of the occurrence of shallow earth-
422 quakes. *Geophysical Journal International*, 55(1):67–86.

423 Kato, A., Obara, K., Igarashi, T., Tsuruoka, H., Nakagawa, S., and Hirata, N. (2012).
424 Propagation of slow slip leading up to the 2011 mw 9.0 tohoku-oki earthquake. *Science*,
425 335(6069):705–708.

426 Liu, Y. and Rice, J. R. (2005). Aseismic slip transients emerge spontaneously in three-
427 dimensional rate and state modeling of subduction earthquake sequences. *Journal of*
428 *Geophysical Research: Solid Earth*, 110(B8).

429 Malin, P. E., Bohnhoff, M., Blümle, F., Dresen, G., Martínez-Garzón, P., Nurlu, M., Ceken,
430 U., Kadiriloglu, F. T., Kartal, R. F., Kilic, T., et al. (2018). Microearthquakes preceding
431 a m4. 2 earthquake offshore istanbul. *Scientific reports*, 8(1):1–11.

432 Marone, C. (1998). The effect of loading rate on static friction and the rate of fault healing
433 during the earthquake cycle. *Nature*, 391(6662):69–72.

434 McLaskey, G. C. (2019). Earthquake initiation from laboratory observations and implica-
435 tions for foreshocks. *Journal of Geophysical Research: Solid Earth*.

436 McMahon, N. D., Aster, R. C., Yeck, W. L., McNamara, D. E., and Benz, H. M. (2017).
437 Spatiotemporal evolution of the 2011 prague, oklahoma, aftershock sequence revealed
438 using subspace detection and relocation. *Geophysical Research Letters*, 44(14):7149–7158.

439 McMahon, N. D., Yeck, W. L., Stickney, M. C., Aster, R. C., Martens, H. R., and Benz,
440 H. M. (2019). Spatiotemporal analysis of the foreshock–mainshock–aftershock sequence
441 of the 6 july 2017 m w 5.8 lincoln, montana, earthquake. *Seismological Research Letters*,
442 90(1):131–139.

443 Mignan, A. (2014). The debate on the prognostic value of earthquake foreshocks: A meta-
444 analysis. *Scientific reports*, 4:4099.

445 Mogi, K. (1963). Some discussions on aftershocks, foreshocks and earthquake swarms:
446 the fracture of a semi-infinite body caused by an inner stress origin and its relation to
447 the earthquake phenomena (third paper). *Bulletin of the Earthquake Research Institute,*
448 *University of Tokyo*, 41(3):615–658.

449 Molchanov, O., Hayakawa, M., Oudoh, T., and Kawai, E. (1998). Precursory effects in the
450 subionospheric vlf signals for the kobe earthquake. *Physics of the Earth and Planetary*
451 *Interiors*, 105(3-4):239–248.

452 Papazachos, B. (1975). Foreshocks and earthquake prediction. *Tectonophysics*, 28(4):213–
453 226.

454 Pedregosa, F., Varoquaux, G., Gramfort, A., Michel, V., Thirion, B., Grisel, O., Blondel,
455 M., Prettenhofer, P., Weiss, R., Dubourg, V., Vanderplas, J., Passos, A., Cournapeau,
456 D., Brucher, M., Perrot, M., and Duchesnay, E. (2011). Scikit-learn: Machine learning
457 in Python. *Journal of Machine Learning Research*, 12:2825–2830.

458 Poli, P., Marguin, V., Wang, Q., Dagostino, N., and Johnson, P. (2020a). Seasonal and co-
459 seismic velocity variation in the region of laquila from single station measurements and
460 implications for crustal rheology. *Journal of Geophysical Research: Solid Earth*, page
461 e2019JB019316.

462 Poli, P., Soaga, J., Molinari, I., Cascone, V., and Boschi, L. (2020b). The 2020 coronavirus
463 lockdown and seismic monitoring of anthropic activities in northern italy. *Sci Rep*, 10:–.

464 Reasenber, P. A. (1999). Foreshock occurrence before large earthquakes. *Journal of*
465 *Geophysical Research: Solid Earth*, 104(B3):4755–4768.

466 Renard, F., McBeck, J., Kandula, N., Cordonnier, B., Meakin, P., and Ben-Zion, Y. (2019).
467 Volumetric and shear processes in crystalline rock approaching faulting. *Proceedings of*
468 *the National Academy of Sciences*, 116(33):16234–16239.

469 Rikitake, T. (1975). Earthquake precursors. *Bulletin of the Seismological Society of Amer-*
470 *ica*, 65(5):1133–1162.

471 Roberts, G. P. and Michetti, A. M. (2004). Spatial and temporal variations in growth rates
472 along active normal fault systems: an example from the lazio–abruzzo apennines, central
473 italy. *Journal of Structural Geology*, 26(2):339–376.

474 Rubin, A. M. and Ampuero, J.-P. (2005). Earthquake nucleation on (aging) rate and state
475 faults. *Journal of Geophysical Research: Solid Earth*, 110(B11).

476 Ruiz, S., Aden-Antoniow, F., Baez, J., Otarola, C., Potin, B., del Campo, F., Poli, P.,
477 Flores, C., Satriano, C., Leyton, F., et al. (2017). Nucleation phase and dynamic inversion
478 of the mw 6.9 valparaíso 2017 earthquake in central chile. *Geophysical Research Letters*,
479 44(20):10–290.

480 Ruiz, S., Metois, M., Fuenzalida, A., Ruiz, J., Leyton, F., Grandin, R., Vigny, C.,
481 Madariaga, R., and Campos, J. (2014a). Intense foreshocks and a slow slip event preceded
482 the 2014 iquique mw 8.1 earthquake. *Science*, 345(6201):1165–1169.

483 Ruiz, S., Metois, M., Fuenzalida, A., Ruiz, J., Leyton, F., Grandin, R., Vigny, C.,
484 Madariaga, R., and Campos, J. (2014b). Intense foreshocks and a slow slip event preceded
485 the 2014 iquique mw 8.1 earthquake. *Science*, 345(6201):1165–1169.

486 Savage, H. M., Keranen, K. M., P. Schaff, D., and Dieck, C. (2017). Possible precursory
487 signals in damage zone foreshocks. *Geophysical Research Letters*, 44(11):5411–5417.

488 Schoenball, M. and Ellsworth, W. L. (2017). A systematic assessment of the spatiotemporal
489 evolution of fault activation through induced seismicity in oklahoma and southern kansas.
490 *Journal of Geophysical Research: Solid Earth*, 122(12):10–189.

491 Schurr, B., Asch, G., Hainzl, S., Bedford, J., Hoechner, A., Palo, M., Wang, R., Moreno,

M., Bartsch, M., Zhang, Y., et al. (2014). Gradual unlocking of plate boundary controlled initiation of the 2014 iquique earthquake. *Nature*, 512(7514):299–302.

Shelly, D. R., Beroza, G. C., and Ide, S. (2007). Complex evolution of transient slip derived from precise tremor locations in western shikoku, japan. *Geochemistry, Geophysics, Geosystems*, 8(10).

Shelly, D. R. and Hardebeck, J. L. (2019). Illuminating faulting complexity of the 2017 yellowstone maple creek earthquake swarm. *Geophysical Research Letters*, 46(5):2544–2552.

Shen, Z.-K., Jackson, D. D., Feng, Y., Cline, M., Kim, M., Fang, P., and Bock, Y. (1994). Postseismic deformation following the landers earthquake, california, 28 june 1992. *Bulletin of the Seismological Society of America*, 84(3):780–791.

Singh, R. P., Mehdi, W., Gautam, R., Senthil Kumar, J., Zlotnicki, J., and Kafatos, M. (2010). Precursory signals using satellite and ground data associated with the wenchuan earthquake of 12 may 2008. *International Journal of Remote Sensing*, 31(13):3341–3354.

Stein, R. S. and Lisowski, M. (1983). The 1979 homestead valley earthquake sequence, california: Control of aftershocks and postseismic deformation. *Journal of Geophysical Research: Solid Earth*, 88(B8):6477–6490.

Tape, C., Holtkamp, S., Silwal, V., Hawthorne, J., Kaneko, Y., Ampuero, J. P., Ji, C., Ruppert, N., Smith, K., and West, M. E. (2018). Earthquake nucleation and fault slip complexity in the lower crust of central alaska. *Nature Geoscience*, 11(7):536–541.

Tramutoli, V., Corrado, R., Filizzola, C., Genzano, N., Lisi, M., and Pergola, N. (2015). From visual comparison to robust satellite techniques: 30 years of thermal infrared satellite data analyses for the study of earthquake preparation phases. *Bollettino di Geofisica Teorica ed Applicata*, 56(2).

516 Trugman, D. T., Ross, Z. E., and Johnson, P. A. (2020). Imaging stress and fault-
517 ing complexity through earthquake waveform similarity. *Geophysical Research Letters*,
518 47(1):e2019GL085888.

519 Virk, H. and Walia, V. (2001). Helium/radon precursory signals of chamoli earthquake,
520 india. *Radiation measurements*, 34(1-6):379–384.

521 Waldhauser, F. (2001). hypodda program to compute double-difference hypocenter loca-
522 tions (hypodd version 1.0-03/2001). *US Geol. Surv. Open File Rep.*, 01, 113.

523 Ward Jr, J. H. (1963). Hierarchical grouping to optimize an objective function. *Journal of*
524 *the American statistical association*, 58(301):236–244.

525 Wehling-Benatelli, S., Becker, D., Bischoff, M., Friederich, W., and Meier, T. (2013). In-
526 dications for different types of brittle failure due to active coal mining using waveform
527 similarities of induced seismic events. *Solid Earth*, 4(2).

528 Wessel, P. and Smith, W. H. (1998). New, improved version of generic mapping tools
529 released. *Eos, Transactions American Geophysical Union*, 79(47):579–579.

530 Westaway, R. (1992). Seismic moment summation for historical earthquakes in italy: tec-
531 tonic implications. *Journal of Geophysical Research: Solid Earth*, 97(B11):15437–15464.

532 Yoon, C. E., Yoshimitsu, N., Ellsworth, W. L., and Beroza, G. C. (2019). Foreshocks and
533 mainshock nucleation of the 1999 m w 7.1 hector mine, california, earthquake. *Journal*
534 *of Geophysical Research: Solid Earth*, 124(2):1569–1582.

535 Zang, A., Christian Wagner, F., Stanchits, S., Dresen, G., Andresen, R., and Haidekker,
536 M. A. (1998). Source analysis of acoustic emissions in aue granite cores under symmetric
537 and asymmetric compressive loads. *Geophysical Journal International*, 135(3):1113–1130.

Figure Captions

Figure 1. Regional map of the study area. The yellow square inside the small map inset on the left corresponds to the central region of Italy represented in the larger topographic map. The small map inset on the right represents magnification of the black dashed area around the epicentral location (red star). The color code used in the map view on the right represents the estimated depth of the foreshock and aftershock activity (estimated in this study: 714 events). The yellow circle represents Balsorano city, and the white triangles represent the stations used in this study. The dashed lines in the right inset map represent the directions A-A' (along strike) and B-B' (normal to the strike) illustrated in the cross sections of Figure 5.

Figure 2. (a) Spectrogram on VVLD.HHZ. The white line is the median of the energy in the frequency band between 5 Hz and 20 Hz calculated within a 1-h sliding window. (b) Blue, cumulative events for the same time period of the experiment; orange, recurrence time for the newly detected events. (c) Estimated magnitudes for the newly detected events. A gap in the continuous data at this receiver location is seen for the night of November 8 to 9, 2019.

Figure 3. Illustration of the waveform-based hierarchical clustering output. (a) Pairwise correlation coefficients between the waveforms for the vertical component of station VVLD (Fig. 1) of the 714 detected events. This matrix is used to perform the hierarchical clustering. (b) Cumulative events combined with the results from the hierarchical clustering, according to the color code in the legend. (c) Characteristic normalized waveforms (vertical component) of the five different clusters revealed in the earthquake sequence. These traces are obtained after stacking all of the individually normalized waveforms belonging to each

cluster.

Figure 4. Spatio-temporal evolution of the earthquake sequences with respect to the mainshock origin time and hypocenter. Left column: Temporal density (number of events per hour). The coefficients of variation (COV) from the recurrence times are indicated for each cluster. Black dashed line, mainshock hypocenter and origin time. Center column: Distance in time and space from each event of the sequence with respect to the mainshock location and origin time. Black dashed line, mainshock hypocenter and origin time. Right column: Spatial density (concentration of events per 0.1 km). Solid line, where 90% of the seismic activity is concentrated. (a)-(e) Each of the five clusters. The same color code from Figure 3 is used.

Figure 5. Map view (left column), and cross-sections along the strike (middle column) and normal-strike (right column) directions for each of the five clusters identified in the sequence (as indicated). All of the locations are relative to the mainshock hypocenter (41.7746°N 13.6066°E ; 13.94 km depth, black star). In all of the panels, the same color code is used as in Figures 3 and 4 to represent each different cluster. The solid black line represents a fault plane of 1 km^2 with the geometry of the second nodal plane (Supplementary Materials Table S1). The directions A-A' (along strike) and B-B' (normal to the strike) are the same as in Figure 1.

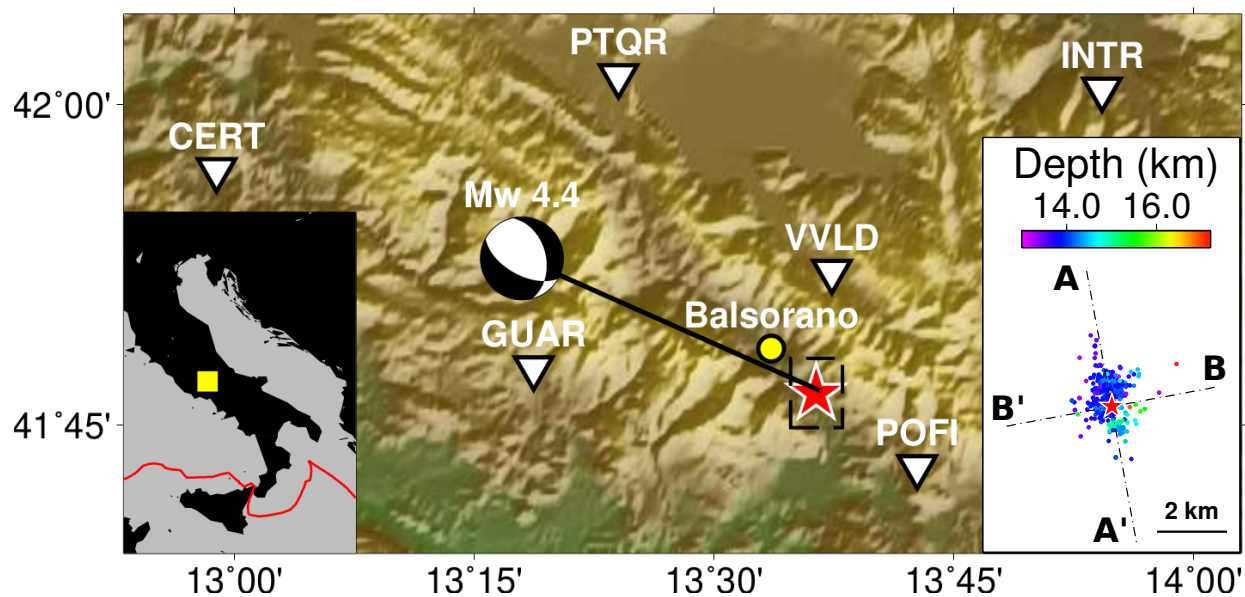


Figure 1: Regional map of the study area. The yellow square inside the small map inset on the left corresponds to the central region of Italy represented in the larger topographic map. The small map inset on the right represents magnification of the black dashed area around the epicentral location (red star). The color code used in the map view on the right represents the estimated depth of the foreshock and aftershock activity (estimated in this study: 714 events). The yellow circle represents Balsorano city, and the white triangles represent the stations used in this study. The dashed lines in the right inset map represent the directions A-A' (along strike) and B-B' (normal to the strike) illustrated in the cross sections of Figure 5.

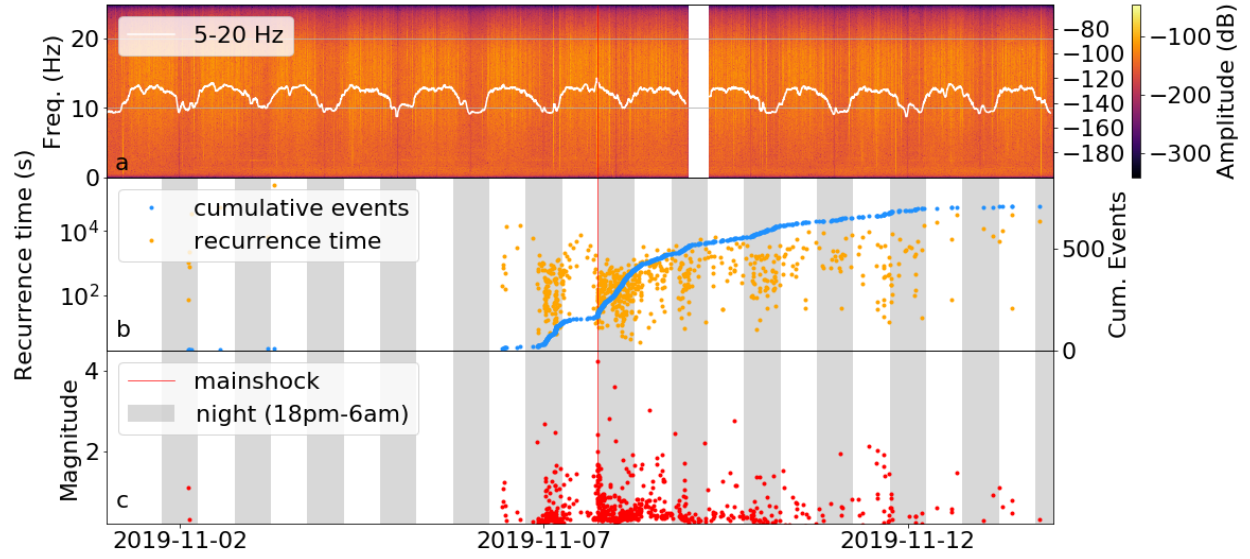


Figure 2: (a) Spectrogram on VVLD.HHZ. The white line is the median of the energy in the frequency band between 5 Hz and 20 Hz calculated within a 1-h sliding window. (b) Blue, cumulative events for the same time period of the experiment; orange, recurrence time for the newly detected events. (c) Estimated magnitudes for the newly detected events. A gap in the continuous data at this receiver location is seen for the night of November 8 to 9, 2019.

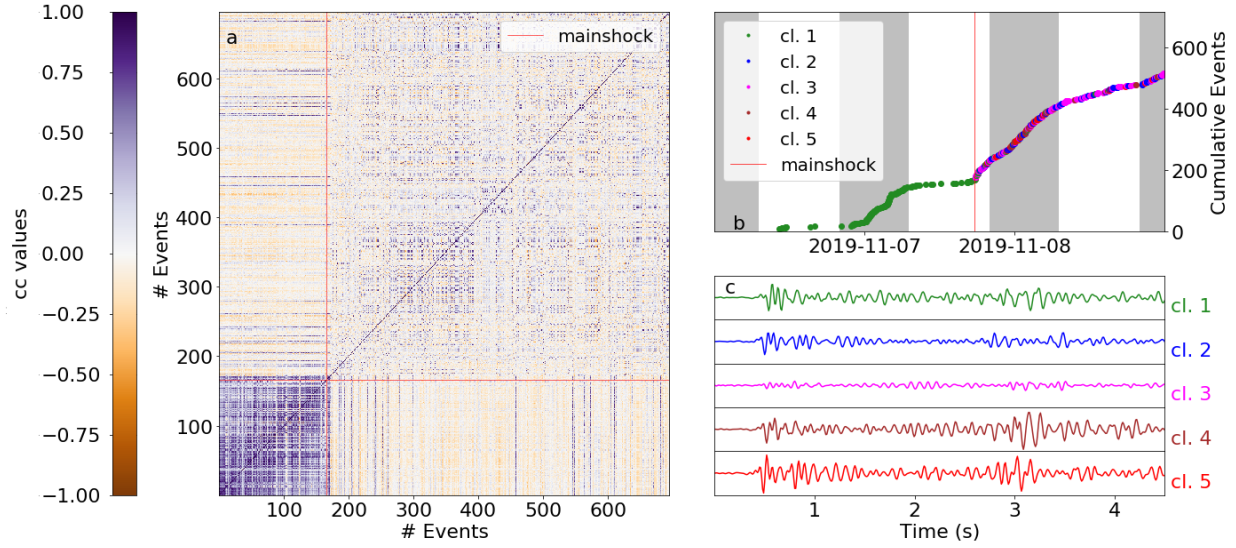


Figure 3: Illustration of the waveform-based hierarchical clustering output. (a) Pairwise correlation coefficients between the waveforms for the vertical component of station VVLD (Fig. 1) of the 714 detected events. This matrix is used to perform the hierarchical clustering. (b) Cumulative events combined with the results from the hierarchical clustering, according to the color code in the legend. (c) Characteristic normalized waveforms (vertical component) of the five different clusters revealed in the earthquake sequence. These traces are obtained after stacking all of the individually normalized waveforms belonging to each cluster.

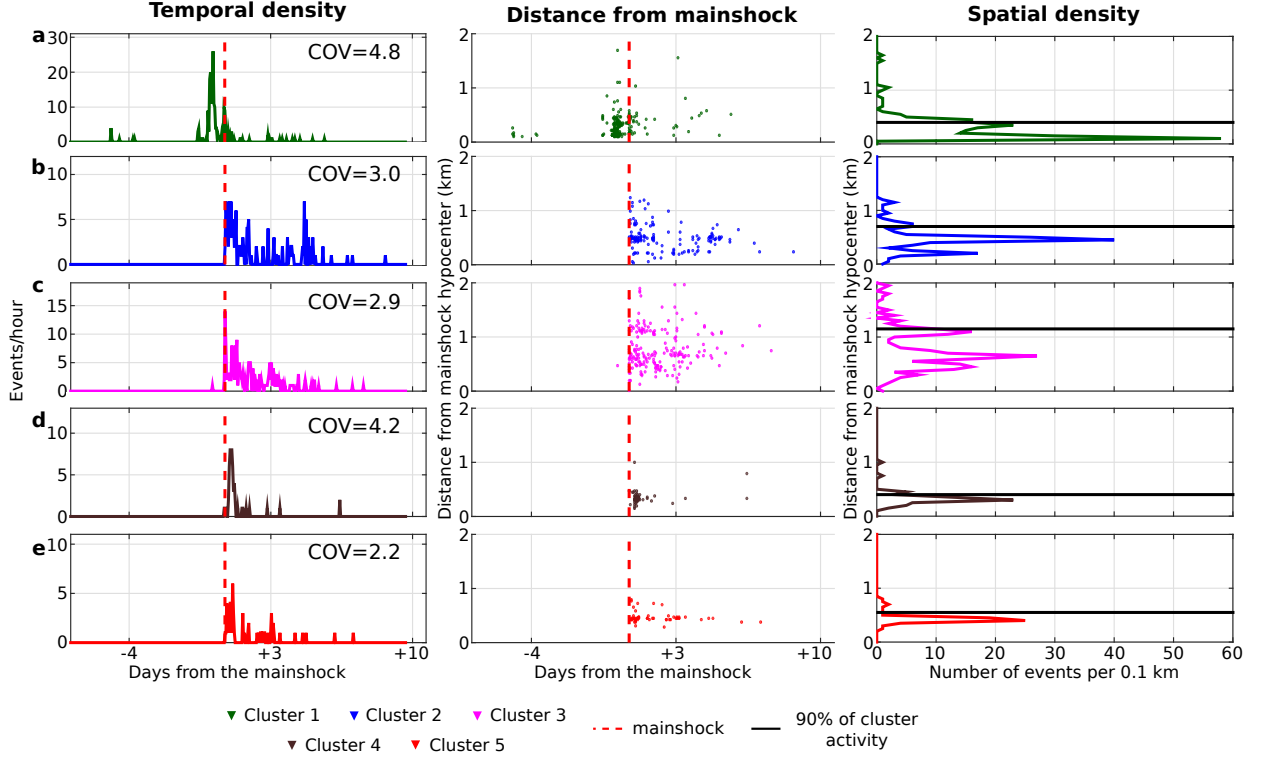


Figure 4: Spatio-temporal evolution of the earthquake sequences with respect to the mainshock origin time and hypocenter. Left column: Temporal density (number of events per hour). The coefficients of variation (COV) from the recurrence times are indicated for each cluster. Black dashed line, mainshock hypocenter and origin time. Center column: Distance in time and space from each event of the sequence with respect to the mainshock location and origin time. Black dashed line, mainshock hypocenter and origin time. Right column: Spatial density (concentration of events per 0.1 km). Solid line, where 90% of the seismic activity is concentrated. (a)-(e) Each of the five clusters. The same color code from Figure 3 is used.

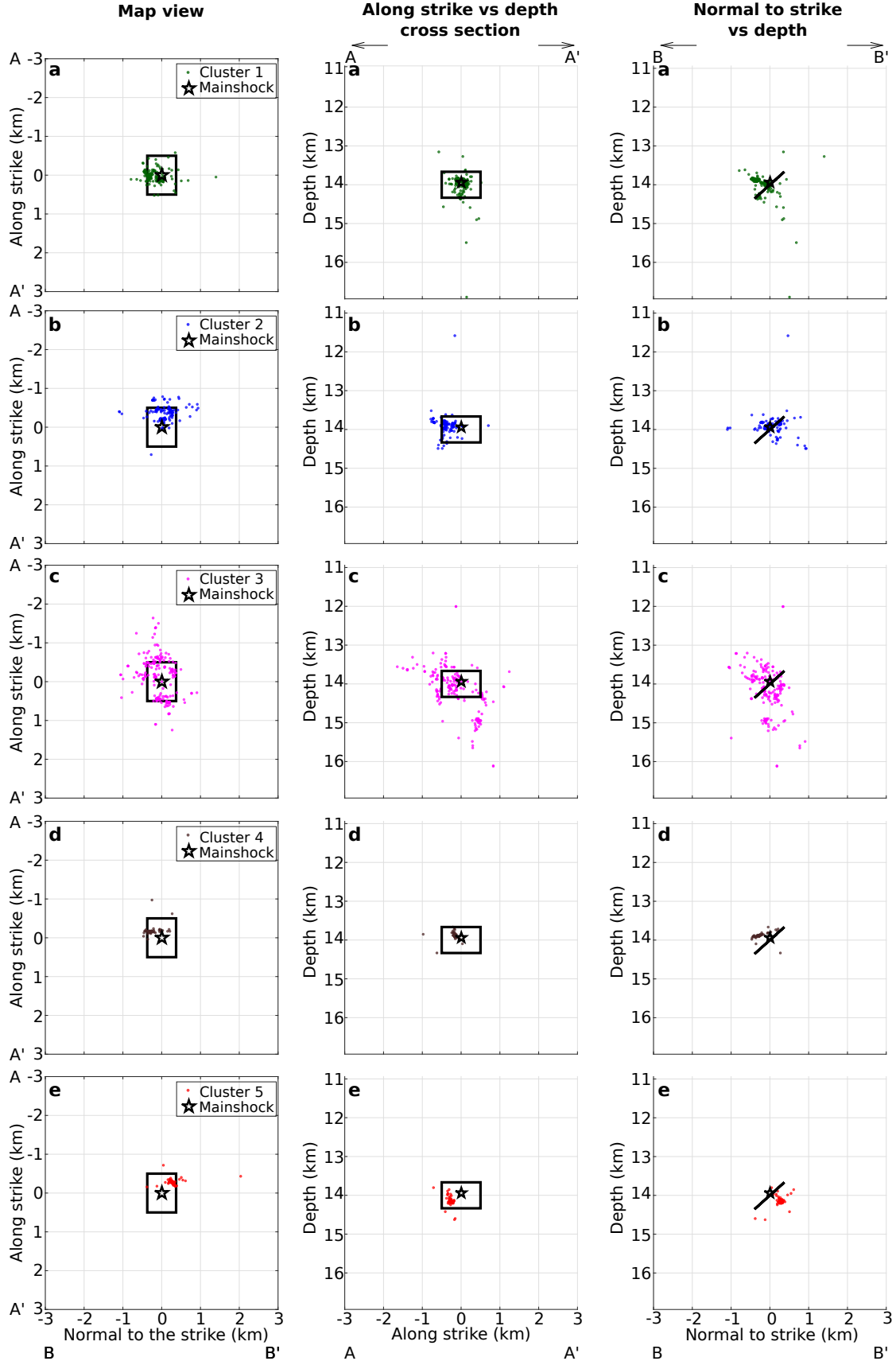


Figure 5: Map view (left column), and cross-sections along the strike (middle column) and normal-strike (right column) directions for each of the five clusters identified in the sequence (as indicated). All of the locations are relative to the mainshock hypocenter (41.7746°N